

Direct numerical simulation of spiral turbulence

S. DONG[†] AND X. ZHENG

Center for Computational and Applied Mathematics, Department of Mathematics,
Purdue University, West Lafayette, IN 47907, USA

(Received 17 February 2010; revised 28 August 2010; accepted 30 August 2010;
first published online 13 December 2010)

In this paper, we present results of three-dimensional direct numerical simulations of the spiral turbulence phenomenon in a range of moderate Reynolds numbers, in which alternating intertwined helical bands of turbulent and laminar fluids co-exist and propagate between two counter-rotating concentric cylinders. We show that the turbulent spiral is comprised of numerous small-scale azimuthally elongated vortices, which align into and collectively form the barber-pole-like pattern. The domain occupied by such vortices in a plane normal to the cylinder axis resembles a ‘crescent moon’, a shape made well known by Van Atta with his experiments in the 1960s. The time-averaged mean velocity of spiral turbulence is characterized in the radial–axial plane by two layers of axial flows of opposite directions. We also observe that, as the Reynolds number increases, the transition from spiral turbulence to featureless turbulence does not occur simultaneously in the whole domain, but progresses in succession from the inner cylinder towards the outer cylinder. Certain aspects pertaining to the dynamics and statistics of spiral turbulence and issues pertaining to the simulation are discussed.

Key words: intermittency, turbulence simulation

1. Introduction

The present study concerns the so-called *spiral turbulence*, a phenomenon observed at moderate Reynolds numbers in the flow between two concentric cylinders (i.e. Taylor–Couette geometry) rotating in opposite directions. Spiral turbulence is prominently characterized by the stable co-existence of laminar and turbulent domains, spatiotemporal intermittency and amazing pattern formations. Alternating intertwined helical stripes, i.e. barber-pole-like patterns, of turbulent and laminar fluids propagate around the cylinder gap and also along the axial direction. Figure 1 shows such a pattern obtained from our simulations; see table 1 for an explanation of the parameters. The fundamental importance of spiral turbulence to the understanding of transition, pattern formation and spatiotemporal intermittency, and its visual appeal, have attracted researchers for the past few decades (Coles 1965; Van Atta 1966; Andereck, Liu & Swinney 1986; Hegseth *et al.* 1989; Colovas & Andereck 1997; Goharzadeh & Mutabazi 2001; Prigent *et al.* 2002; Meseguer *et al.* 2009; Dong 2009*b*).

The spatiotemporal intermittency exhibited by spiral turbulence has also been observed in other types of flows, most notably in the plane- and torsional-Couette flows (Bottin *et al.* 1998; Cros & Gal 2002; Prigent *et al.* 2002; Barkley & Tuckerman

[†] Email address for correspondence: sdong@math.purdue.edu

Symbol	Definition	Symbol	Definition
R_i	Radius of inner cylinder	Ω_i	Angular velocity of inner cylinder
R_o	Radius of outer cylinder	Ω_o	Angular velocity of outer cylinder
L_z	Axial dimension of domain	U_i	Rotation velocity of inner cylinder, $U_i = \Omega_i R_i$
η	Radius ratio, $\eta = R_i/R_o$	U_o	Rotation velocity of outer cylinder, $U_o = \Omega_o R_o$
d	Gap width, $d = R_o - R_i$	Re_i	Inner-cylinder Reynolds number, $Re_i = U_i d/\nu$
Γ	Aspect ratio, $\Gamma = L_z/d$	Re_o	Outer-cylinder Reynolds number, $Re_o = U_o d/\nu$
ν	Kinematic viscosity of fluid		

TABLE 1. Definitions of geometric and dynamical parameters.

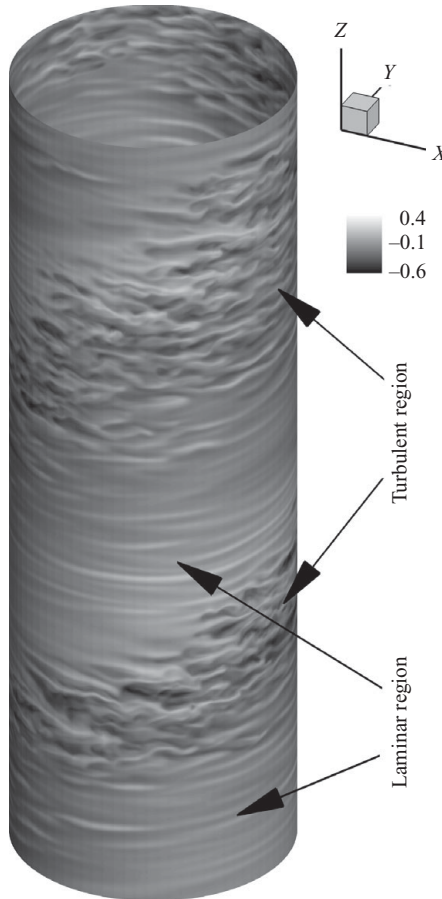


FIGURE 1. Contours of instantaneous azimuthal velocity in a cylindrical grid surface showing barber-pole-like patterns formed by turbulent and laminar regions. ($Re_i = 611$, $Re_o = -1375$, $\Gamma = 50.2$.) See table 1 for definitions of the parameters.

2005; Lepiller *et al.* 2007). The co-existence of two distinct dynamical states at the same values of the control parameters has also been found in other kinds of dynamical systems; see Cross & Hohenberg (1993) and Berge, Pomeau & Vidal (1984) for a review of related aspects.

Source	η	Γ	Re_i	Re_o
Coles (1965)	0.874, 0.889	13.95, 15	0–15 000	–10 000 to –80 000
Van Atta (1966)	0.889	8.5–13.75	–10 000 to 20 000	–10 000 to –170 000
Coles & Van Atta (1966)	0.889	?	–5600	50 000
Coles & Van Atta (1967)	0.889	?	–5600 (?)	50 000 (?)
Andereck <i>et al.</i> (1986)	0.883	20–48	500–1800	–800 to –4000
Hegseth <i>et al.</i> (1989)	0.882	$\lesssim 73$	770, 950	< –4000
Litschke & Roesner (1998)	0.789, 0.895	68.5 (?)	450–1400 (?)	–600 to –3100 (?)
Goharzadeh & Mutabazi (2001)	0.88	46	520–700	–1260 to –1683
Prigent <i>et al.</i> (2002)	0.983	430	450–810 (?)	–600 to –1200 (?)
Prigent <i>et al.</i> (2003)	0.983	442	450–800 (?)	–600 to –1200 (?)
Goharzadeh & Mutabazi (2008)	0.88	46	680	–1380
Meseguer <i>et al.</i> (2009)	0.883	29.9	540–640, 575–900	–1200, –3000
Dong (2009 <i>b</i>)	0.89	6–25	530–900	–1375

TABLE 2. Global parameters in existing studies of spiral turbulence. The values followed by a question mark (?) may not be exact because they are not available from the text and are read from the figures.

It is appropriate to first define several parameters before proceeding further. The problem focused on is the incompressible flow between two long concentric cylinders which revolve around their common axis in opposite directions. Table 1 summarizes several geometric and dynamical parameters involved in the problem. There are two main geometric parameters, the radius ratio η and the aspect ratio Γ . The rotations of the two cylinders are assumed to be independent, with constant angular velocities Ω_i and Ω_o . The inner- and outer-cylinder Reynolds numbers (Re_i and Re_o) are, respectively, defined based on the two rotation velocities.

The existing experimental and computational studies of spiral turbulence are listed in table 2, in which we summarize the global parameters including the radius ratio, aspect ratio and the inner-/outer-cylinder Reynolds numbers. We next summarize the main results from these studies.

The earliest observations of spiral turbulence are documented in the works of Coles and Van Atta (Coles 1965; Van Atta 1966; Coles & Van Atta 1966, 1967). These early experiments were conducted with an outer-cylinder Reynolds number Re_o of the order –10 000 to –80 000, considerably larger than those of subsequent investigations. Major observations from these studies include: (i) the spiral pattern rotates at nearly the mean angular velocity of the two cylinders (Coles 1965; Van Atta 1966); (ii) spiral turbulence can be observed in situations when the cylinders rotate in opposite directions (counter-rotating), or when the inner one is at rest, or even when the two rotate in the same direction (co-rotating), provided that sufficiently strong disturbances are present (Coles 1965); (iii) the mean shape of the interface between the turbulent and laminar regions in a horizontal plane (normal to the cylinder axis) resembles a ‘crescent moon’, with its leading and trailing interfaces, respectively, located near the outer and inner cylinder walls (Van Atta 1966). This shape in the horizontal plane has been reproduced in numerical simulations recently by Dong (2009*b*) using conditionally averaged statistics, in which the three-dimensional mean interface between turbulent and laminar spirals has also been characterized.

The experiment of Andereck *et al.* (1986) provides a comprehensive overview of various regimes of the counter-rotating Taylor–Couette flow as well as the co-rotating flow at radius ratio 0.883. The range of parameters in the (Re_i , Re_o) plane that lead to different regimes has been determined. Pertaining to spiral turbulence, it is

observed that the angular frequency of the spiral pattern can be best described by $C\Omega_o$ (where $C < 1$ is a constant and possibly Re_o dependent) under the experimental conditions, and has essentially no dependence on Ω_i . Hysteresis has been documented. It is also observed that, at sufficiently high Re_o values and when the inner-cylinder rotation is accelerated rapidly, the left- and right-handed turbulent spirals can exist simultaneously, joining near the mid-height of cylinder and forming a V-shaped pattern. Andereck *et al.* (1986) have also provided several stunning experimental visualizations of spiral turbulence.

Certain properties of the turbulent spirals have been investigated by several subsequent studies. For example, a variation in the spiral pitch angle along the axial direction is observed when the experimental boundary conditions at the two ends of the cylinders are changed (rigid or free endwalls) (Hegseth *et al.* 1989), and is modelled using a kinematic phase equation. Several parameters involved in the phase equation, such as the diffusion coefficient, have been recently measured experimentally (Goharzadeh & Mutabazi 2008). Measurements of the turbulent fraction and related parameters in the spiral turbulence regime are reported in Goharzadeh & Mutabazi (2001). Spiral turbulence has also been used as a benchmark problem for testing experimental techniques (Litschke & Roesner 1998), in which among other points significant influence of the end plates on the local flow field has been noted.

Prigent *et al.* (2002, 2003) have described a unique set of experiments on the Taylor–Couette flow (and also plane-Couette flow). The uniqueness lies in large aspect ratios, which are considerably larger compared to previous experiments; see table 2. The radius ratio used in this experiment is also notably higher compared to other experiments. Starting from the fully turbulent state, as the Reynolds number is decreased a long-wavelength modulation to the turbulent intensity is observed from these experiments, which leads to a striped pattern in the flow. Spiral turbulence is suggested to be the ultimate stage of this modulation as the Reynolds number is decreased. Prigent *et al.* also observe that the turbulent intensity modulation can be modelled using the coupled Ginzburg–Landau equations with noise.

The above studies are all experimental investigations. Computations of spiral turbulence have appeared only very recently. Two independent simulations of spiral turbulence, one from a group in Europe (Meseguer *et al.* 2009) and one from our group (Dong 2009*b*), appeared last year. These two studies were presented at the 16th International Couette–Taylor Workshop (Marques *et al.* 2009; Dong 2009*a*). Meseguer *et al.* (2009) have explored the parameter space at two outer-cylinder Reynolds numbers, and observed axial vortex filaments in the annular domain that are generated near the inner cylinder and gradually spread out downstream towards the outer cylinder. On the other hand, Dong (2009*b*) has employed conditional averaging techniques in the simulations and concentrated on the conditionally averaged statistics of spiral turbulence. Dong (2009*b*) has made three observations: (i) a significant azimuthal gradient of the conditional mean velocity persists across turbulent and laminar spiral regions; (ii) the cores of turbulent and laminar spirals are demarcations of axially opposite flows in the mean sense; (iii) spiral turbulence exhibits distinct distribution characteristics in turbulent intensity compared to fully developed turbulence.

Employing detailed three-dimensional direct numerical simulations (DNS), this paper presents a comprehensive study of the flow structures and dynamical features, together with the *ordinarily* time-averaged statistical features, of spiral turbulence. By ‘ordinary’ time averaging, we refer to the direct averaging of the flow field in time, which is different from the conditional averaging employed by Dong (2009*b*). The

problem setting is the counter-rotating configuration of the Taylor–Couette geometry at a radius ratio $\eta = 0.89$, chosen in accordance with Dong (2009*b*). The majority of results are for an aspect ratio $\Gamma = 25.1$. A larger aspect ratio $\Gamma = 50.2$ has also been simulated. For spiral turbulence, we have concentrated on two moderate Reynolds numbers, $Re_i = 611$ and 700 (with a fixed $Re_o = -1375$), which lead to regular turbulent and laminar spiral patterns. The present study has revealed several characteristics of spiral turbulence that were unknown before. In particular, the turbulent spiral is shown to be comprised of a large number of small-scale azimuthal vortices, which align themselves and collectively form the spiral pattern. The laminar spiral region is found not to be void of vortices, but teems with pairs of azimuthal vortices that are confined to the linearly unstable layer near the inner cylinder wall. We also observe that the left-handed and right-handed spiral patterns leave quite different statistical footprints, despite the common features they share. We will also compare and relate aspects of the ordinarily time-averaged flow statistics studied here to the conditionally averaged statistics in Dong (2009*b*).

2. Numerical issues: convergence, consistency and validation

We consider the incompressible flow between two counter-rotating concentric cylinders. The cylinders have an axial dimension L_z , and the flow is assumed to be periodic at both ends of the cylinders. This setting can be used to approximate the situation with two infinitely long cylinders. The cylinder axis is assumed to coincide with the z -axis, and the two cylinder ends are located at $z = 0$ and L_z , respectively. The inner and outer cylinders revolve around their common axis at constant angular velocities, denoted by Ω_i ($\Omega_i > 0$) and Ω_o ($\Omega_o < 0$), respectively, with the convention that a positive (negative) angular velocity represents counter-clockwise (clockwise) rotations when viewing towards the $-z$ direction.

The problem is described by the three-dimensional incompressible Navier–Stokes equations. Our numerical scheme for solving these equations employs a hybrid spectral/spectral-element approach, as detailed in previous works (Dong & Karniadakis 2005; Dong *et al.* 2006; Dong 2007, 2008). In brief, the flow variables are discretized with a Fourier spectral expansion in the axial (z)-direction and a high-order spectral element expansion in the annular domain of the x – y plane. Therefore, we will subsequently refer to Fourier planes or spectral elements from time to time. Temporal discretization of the Navier–Stokes equations is through a velocity-correction-type scheme with second-order accuracy (Karniadakis, Israeli & Orszag 1991). The algorithms for parallel processing in our solver have been described in Dong & Karniadakis (2004) and Dong, Karniadakis & Karonis (2005). No-slip boundary conditions are imposed on the two cylinder walls to realize their rotation velocity conditions. In the simulations, the length is normalized by the inner cylinder radius R_i ; the velocity is normalized by a unit velocity U_d , and the pressure is normalized by ρU_d^2 , where ρ is the fluid density.

The radius ratio considered in this paper is fixed at $\eta = 0.89$ (with $R_i = 1.0$ and $R_o = 1.125$). Throughout the simulation, the outer-cylinder Reynolds number is fixed at $Re_o = -1375$. Several inner-cylinder Reynolds numbers have been simulated, which as identified in Dong (2009*b*) accommodate regular turbulent/laminar spiral patterns for the range $611 \lesssim Re_i \lesssim 700$. The main results on spiral turbulence presented here are for $Re_i = 611$ and 700 . Two other Re_i values outside the spiral turbulence regime have also been considered ($Re_i = 530$ and 800). The majority of results are with an aspect ratio $\Gamma = 25.1$, where a single period of the spiral pattern along the axial

Case	Γ	N_z	Element order
A	12.6	384	6
B	18.9	384	6
C	25.1	512	6
D	25.1	512	7
E	25.1	512	8
F	25.1	512	9

TABLE 3. Grid resolution parameters for the convergence tests in figure 2. N_z denotes the number of Fourier grid points in the z -direction. A total of 640 quadrilateral spectral elements are used in each annular x - y plane.

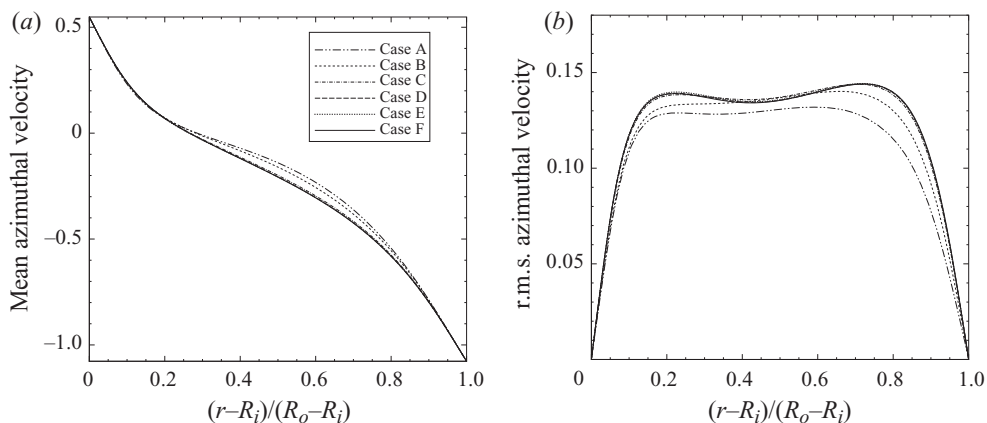


FIGURE 2. Convergence test ($Re_i = 700$, $Re_o = -1375$): profiles of time-averaged mean azimuthal velocity (a) and r.m.s. azimuthal fluctuation velocity (b) for different resolutions. r is the radial coordinate.

direction has been obtained (see §3). Results with a larger aspect ratio, $\Gamma = 50.2$, have also been obtained for $Re_i = 611$, where two periods of the spiral pattern have been realized along the axial direction (figure 1). With $\Gamma = 25.1$, we have obtained a left-handed spiral at $Re_i = 611$ and a right-handed spiral at $Re_i = 700$; on the other hand, at $Re_i = 611$ with $\Gamma = 50.2$ we obtain a right-handed spiral, which is different from that with $\Gamma = 25.1$.

To ensure that our simulation results have converged, we have conducted extensive grid-resolution tests. Figure 2 shows results of the grid-resolution study at $Re_i = 700$. The plots (a) and (b) in the figure, respectively, compare profiles of the time-averaged mean azimuthal velocity and the root-mean-square (r.m.s.) azimuthal fluctuation velocity across the cylinder gap under different grid resolutions (with increasing resolution from case A to case F). The grid resolution parameters for cases A to F are summarized in table 3. In these tests, along the axial direction 512 Fourier planes (i.e. 256 Fourier modes) have been employed in most cases, and 384 Fourier planes have been used for cases A and B. A 3/2-dealiasing has been performed. Within each plane (annular domain), we employ a spectral element mesh with 640 quadrilateral elements, and the element order is varied between 6 and 9, with over-integration (Dong 2007). Figure 2(a,b) shows that the profiles essentially collapse into a single

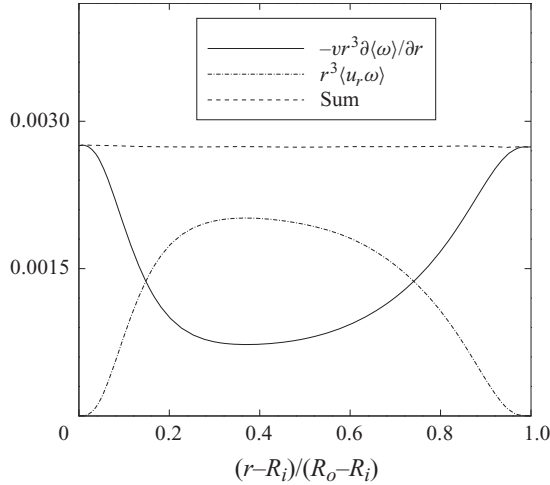


FIGURE 3. Angular velocity current balance ($Re_i = 700$). Note that Re_o is fixed at -1375 throughout this study.

curve as the resolution increases, demonstrating the convergence of the simulation results. For simulations at other Reynolds numbers, we have mostly employed an element order of 8 or 9, and 512 Fourier planes have been used along the axial direction. For the simulation with a larger aspect ratio $\Gamma = 50.2$ at $Re_i = 611$, we have employed 1024 Fourier planes in the axial direction.

To check the internal consistency of our simulation results, we consider the angular velocity current balance relation. It has been shown in Eckhardt, Grossmann & Lohse (2007) that the quantity

$$J^\omega = r^3 \left(\langle u_r \omega \rangle - v \frac{\partial \langle \omega \rangle}{\partial r} \right), \quad (2.1)$$

the so-called angular velocity current, is a constant across the cylinder gap for flows in the Taylor–Couette geometry. In (2.1), r is the radial coordinate, and u_r and ω are, respectively, the radial velocity and the angular velocity; $\langle \cdot \rangle$ denotes the averaging in time and also in the axial and azimuthal directions. Since the terms on the right-hand side can be computed independently, this equation can be used as a consistency check of the results. In figure 3, we plot profiles of the two terms on the right-hand side of (2.1), together with their sum J^ω across the cylinder gap for $Re_i = 700$. One can observe that J^ω computed from the simulation data is virtually a constant across the cylinder gap. This in a sense demonstrates the internal consistency of our simulation results.

Our flow solver has been extensively validated for turbulent Taylor–Couette flows by comparing with the experimental data in previous studies; see Dong (2007) for comparisons in the standard Taylor–Couette setting (i.e. outer cylinder fixed) and Dong (2008) for comparison with the counter-rotating configuration in the fully turbulent regime. Very good agreements are observed in these comparisons.

We next present a further comparison with an experiment for the spiral turbulence regime. A survey of literature indicates that the experimental data for spiral turbulence that can be used for quantitative validation of direct numerical simulations are very scarce. Results of the majority of experiments on spiral turbulence are

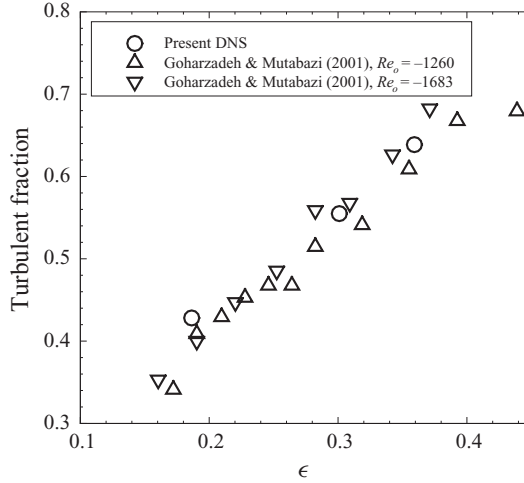


FIGURE 4. Comparison of turbulent fraction between simulation and experiment. The horizontal axis, ϵ , represents the deviation of Re_i from a threshold Reynolds number; see the text for its definition.

qualitative. Some statistical data are available in Van Atta (1966), but the Reynolds numbers in that set of experiments are beyond the reach of current direct numerical simulations (see table 2). As a further validation, here we compare our simulations with the experiment of Goharzadeh & Mutabazi (2001). This experiment was conducted at a comparable radius ratio 0.88 and at comparable Reynolds numbers. In figure 4, we compare the mean turbulent fraction (in mid-gap) for spiral turbulence from the simulation and the experiment, as a function of a dimensionless parameter $\epsilon = (Re_i - Re_i^*)/Re_i^*$, where Re_i^* is the threshold Re_i value at which turbulent bursts start to appear from the laminar background for a fixed Re_o . For $Re_o = -1375$ in the current simulations, we have determined that $Re_i^* \approx 515$. The mean turbulent fraction is defined as the fraction of total duration of turbulent phases in the total duration of the velocity history, or equivalently, the ratio of the total area of the turbulent region to the total area of the space–time diagram. A space–time diagram is a plot in the spatial–temporal plane of the velocity data collected along a fixed line (parallel to cylinder axis) over time. It has often been adopted in experiments (Litschke & Roesner 1998; Goharzadeh & Mutabazi 2001), and can also be obtained from simulations (Dong 2009b). To distinguish the turbulent phase from an instantaneous velocity history, we employ the sum of the normalized r.m.s. velocity squared and velocity time-derivative squared as the criterion. If for a time instant, this quantity is above a cutoff value, it will be marked turbulent. The results of this procedure are verified by visual comparisons with the velocity history to ensure that all significant features have been accounted for. The turbulent fraction data for $Re_o = -1260$ and -1683 are available in Goharzadeh & Mutabazi (2001). It is evident from figure 4 that the turbulent fractions from the current simulation are in good agreement with the experimental data.

The above convergence tests, internal consistency check and comparisons with experimental data provide confidence in the correctness and accuracy of the current simulation results.

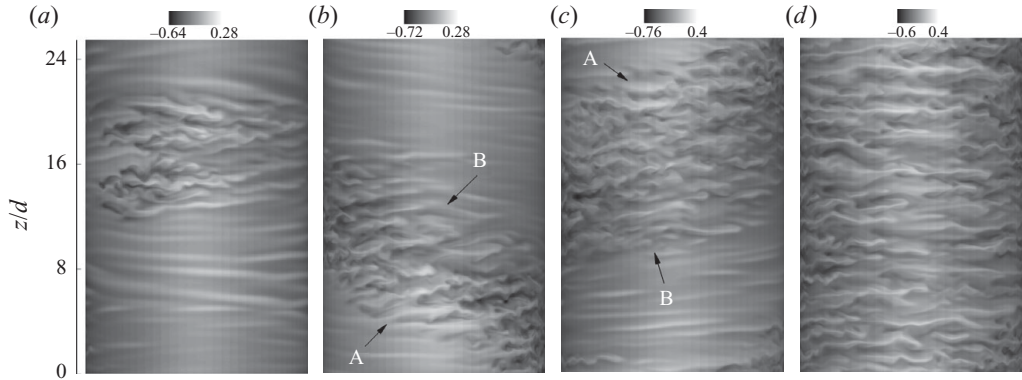


FIGURE 5. Contours of instantaneous azimuthal velocity in a grid surface (essentially cylindrical) near the middle of the cylinder gap at Reynolds numbers $Re_i = 530$ (a), 611 (b), 700 (c) and 800 (d). In (b) and (c) the letters ‘A’ and ‘B’, respectively, point to the leading and trailing edges of the turbulent spiral.

3. Dynamics of spiral turbulence

We have carried out long-time simulations at each Reynolds number, and monitored the global physical parameters such as the torques on the inner and outer cylinders. At the statistically stationary states the torques on the cylinders fluctuate in time, but always around some constant mean level. All results presented below are for the statistically stationary states.

Figure 5 provides an overview of the flow features at several Reynolds numbers within the spiral turbulence regime (plots (b) and (c)) and outside the regime (plots (a) and (d)). Plotted are contours of the instantaneous azimuthal velocity (side view) in a grid surface, which is essentially cylindrical, near the middle of the cylinder gap. Note that the outer-cylinder Reynolds number is fixed at $Re_o = -1375$ in all cases. Figure 5(a) is for $Re_i = 530$, corresponding to the regime of turbulent bursts, also referred to as the intermittency regime or intermittent turbulent spots in the literature. Figures 5(b) and 5(c) are for $Re_i = 611$ and 700, respectively, corresponding to the spiral turbulence regime. Figure 5(d) is for $Re_i = 800$, corresponding to the regime beyond spiral turbulence.

3.1. Turbulent bursts and featureless turbulence

Under current configurations, the turbulent burst regime precedes regular spiral turbulence as Re_i increases. Our simulation shows that localized turbulent patches (bursts) appear from, and disappear into, the otherwise laminar flow background in random locations (figure 5a).

The simulation indicates that the activeness of the turbulent bursts exhibits a quasi-periodic nature in time. For some period of time, the turbulent patches are very active, in the sense that they randomly emerge from, persist in, and then vanish into the laminar flow. We will refer to these periods of time as ‘active phases’. Figure 5(a) is a snapshot of an instant in the active phase. For other periods of time, no turbulent patches exist at all, and the entire flow is completely laminar. We will refer to these periods in time as ‘quiescent phases’. These two clearly identifiable phases are demonstrated in figure 6(a) by the time histories of the torque (x and z components)

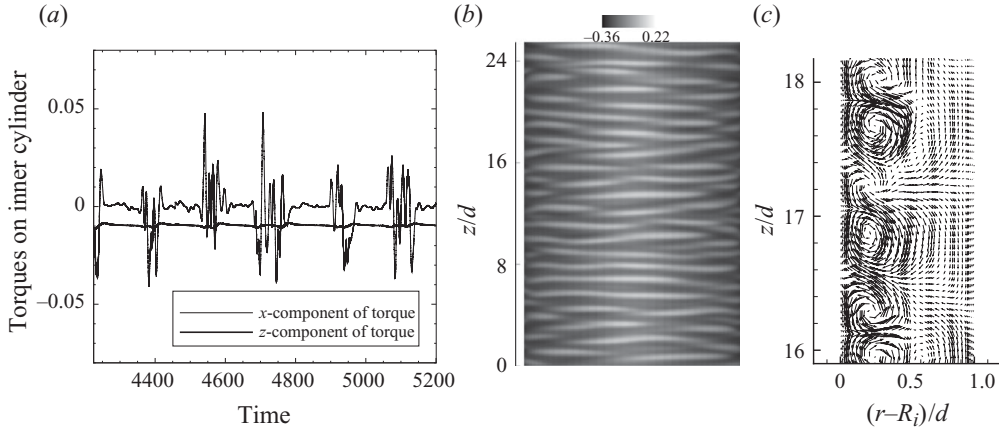


FIGURE 6. Characteristics of turbulent bursts ($Re_i = 530$): (a) time histories of torque components on the inner cylinder wall; (b) contours of azimuthal velocity in a cylindrical grid surface near mid-gap in the quiescent phase; (c) velocity vector map in a radial–axial plane at the same time instant as (b).

acting on the inner cylinder at $Re_i = 530$. The torque vector \mathbf{T} is defined by

$$\mathbf{T} = \int_{\Gamma} \mathbf{x} \times \mathbf{F} d\Gamma, \quad (3.1)$$

where \mathbf{x} is the position vector, and \mathbf{F} is the force (due to pressure and friction) acting on the cylinder surface Γ . The torque that is normally referred to in the Taylor–Couette geometry is the z -component (axial component) of \mathbf{T} . Figure 6(a) shows that the x -component of torque experiences high-frequency large fluctuations at certain periods of time, and is essentially zero at other times. They correspond, respectively, to the active and quiescent phases. The two phases alternate with each other with a period approximately $160R_i/U_d \sim 200R_i/U_d$, considerably larger than the rotation periods of the inner and outer cylinders, which are $15.1R_i/U_d$ and $6.6R_i/U_d$, respectively, at $Re_i = 530$.

Figure 6(b) shows a snapshot of the flow at an instant in the quiescent phase at $Re_i = 530$. Plotted are contours of the azimuthal velocity in the same grid surface as in figure 5(a). One can observe flow structures which are elongated along the azimuthal direction but often appear to be interrupted azimuthally. This is reminiscent of the laminar interpenetrating spirals discussed in Andereck *et al.* (1986). These constitute the main flow structures in the quiescent phase of the turbulent burst regime. Figure 6(c) shows the velocity vector patterns in a radial–axial plane at the same time instant as figure 6(b). It suggests that the laminar interpenetrating spirals are pairs of azimuthal vortices confined to regions near the inner cylinder, not far beyond the linearly unstable region. These vortices appear not dissimilar to the laminar vortices near the inner wall in wide-gap simulations of the counter-rotating Taylor–Couette flow at low Reynolds numbers (Dong 2008).

One can compare the turbulent bursts observed here and those discussed in Coughlin & Marcus (1996). The turbulent patches observed in current simulations are localized in space. Once the active phase starts, they appear in random locations of the flow, while the rest of the flow domain is laminar. In contrast, those discussed in Coughlin & Marcus (1996) are not localized, but space-filling bursts. Once they start, the entire flow domain becomes turbulent. On the other hand, the alternation

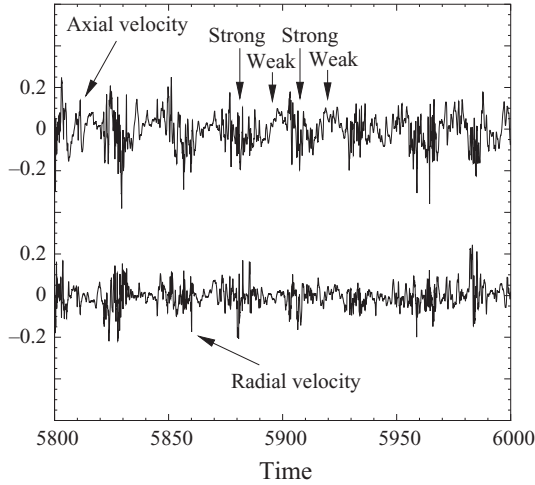


FIGURE 7. Turbulent intensity modulation: time histories of the axial and radial velocities in the middle of the cylinder gap at $Re_i = 800$.

between the active and quiescent phases in time observed in the current simulations appears similar in character to the temporal oscillation between the laminar flow and the turbulent bursts observed in Coughlin & Marcus (1996). However, the oscillation period between the two phases in the current simulations, about 10–13 times the inner-cylinder rotation period, is notably larger than the temporal oscillation period between the laminar and turbulent flows in Coughlin & Marcus (1996), which is about twice the inner-cylinder rotation period.

For a range of moderate Re_i values one can observe alternating regions of turbulent and laminar fluids forming regular helical bands (figure 5*b,c*). These will be the focus of subsequent discussions. Beyond this range of Re_i , the entire flow becomes turbulent, and the whole domain appears permeated with small-scale structures, as shown in figure 5(*d*) for $Re_i = 800$. Examination of the velocity data indicates that these structures are small-scale vortices. They are distributed in the entire annular domain, unlike the laminar vortices at low Re_i , which are confined to the linearly unstable region near the inner cylinder. Because no apparent large-scale features can be discerned, this regime has been called ‘featureless turbulence’ by Andereck *et al.* (1986).

Our simulation results show that in the featureless turbulence regime there exists a notable modulation in the turbulent intensity. This is shown in figure 7, in which we plot the time histories of the axial and radial velocities at a point in the middle of the cylinder gap at $Re_i = 800$. The velocity histories are highly fluctuatory, indicative of the turbulent nature of the flow. A modulation in the fluctuation intensity is clearly visible from the velocity histories. The modulation can also be discerned from the azimuthal velocity component, but not as obviously. The turbulent intensity modulation in the featureless turbulence regime observed here is consistent with the observations in Prigent *et al.* (2002, 2003). By starting from the fully developed turbulent regime and reducing the Reynolds number, Prigent *et al.* observe a continuous transition from turbulence towards a regular pattern of inclined stripes of alternating turbulence strength (i.e. modulation). Spiral turbulence is thought to be the ultimate stage of such a modulation in turbulent intensity. Results from the

current simulations about the turbulent intensity modulation at Reynolds numbers beyond the spiral turbulence regime are consistent with such a scenario.

3.2. Spiral turbulence

We next concentrate on the range of moderate Re_i values at which regular turbulent and laminar spiral patterns can be observed. Discussions below will focus on two Reynolds numbers, $Re_i = 611$ and 700 (with $\Gamma = 25.1$), corresponding to left-handed and right-handed spirals, respectively (figure 5*b,c*). As noted in many previous studies, the spiral pattern revolves around the cylinder gap in the same direction as the outer cylinder, with its shape approximately unchanged. We will distinguish the two edges of the helical band into the leading and trailing edges. In figures 5(*b*) and 5(*c*), the leading and trailing edges of the turbulent spiral are marked by the letters ‘A’ and ‘B’, respectively.

Figures 5(*b*) and 5(*c*) indicate that the turbulent spiral consists of a large number of small-scale structures while the laminar spiral appears largely void of features except for sporadic streaky regions in the domain. A close examination of the flow field, on the other hand, shows that the laminar spiral region also teems with flow structures, albeit only in the region near the inner cylinder wall. Figure 8(*a*) plots the azimuthal velocity contours in a cylindrical grid surface near the inner cylinder (at a distance of approximately $d/6$) at $Re_i = 700$. One can clearly observe long high-speed streaks distributed in the entire laminar spiral region. Some of these streaks have been marked by arrows in the plot.

To understand the nature of the small-scale structures in the turbulent spiral region and the streaks in the laminar spiral, we investigate the velocity patterns in the cylinder gap. Figure 8(*b*) shows the velocity vector map in a radial–axial plane. One can clearly distinguish the cross-sections of the turbulent and laminar spirals. Two magnified plots of the turbulent and laminar regions are also shown in this figure. These data clearly demonstrate that the structures observed in the turbulent spiral region are azimuthal vortices with scales considerably smaller than the cylinder gap. These small-scale turbulent vortices are distributed radially in the entire gap at the core of the turbulent region. Away from the core, they tend to be distributed towards either the inner or the outer cylinder wall. Note that there are two interfaces between the turbulent and laminar regions. One interface is on the side of the leading edge of the turbulent spiral, and the other is on the trailing edge side. The dark arrow in figure 8(*b*) approximately marks the position of the leading edge of the turbulent spiral. The other interface, at the trailing edge of the turbulent spiral, is not visible in figure 8(*b*) due to truncation of the domain in this plot. One can observe from this figure that, towards the laminar–turbulent interface on the leading edge side, the turbulent vortices appear to be mostly distributed towards the outer wall or the outer half of the cylinder gap, while the region towards the inner wall is apparently occupied by the laminar fluid. This is a persistent feature of spiral turbulence, applicable to both right-handed and left-handed spirals. At the laminar–turbulent interface on the trailing edge side (not visible from figure 8(*b*)), this characteristic is reversed. Turbulent vortices tend to be distributed towards the inner wall, while the laminar fluid occupies the region towards the outer wall.

These distribution characteristics of turbulent vortices are intimately correlated with the statistical features of the turbulent spiral observed based on the conditionally averaged statistics (Dong 2009*b*). It is shown in Dong (2009*b*) that the distribution of conditional r.m.s. velocity in the radial axial plane is characterized by two prominent ‘tails’ at the leading and trailing edges of the turbulent spiral. The one at the leading

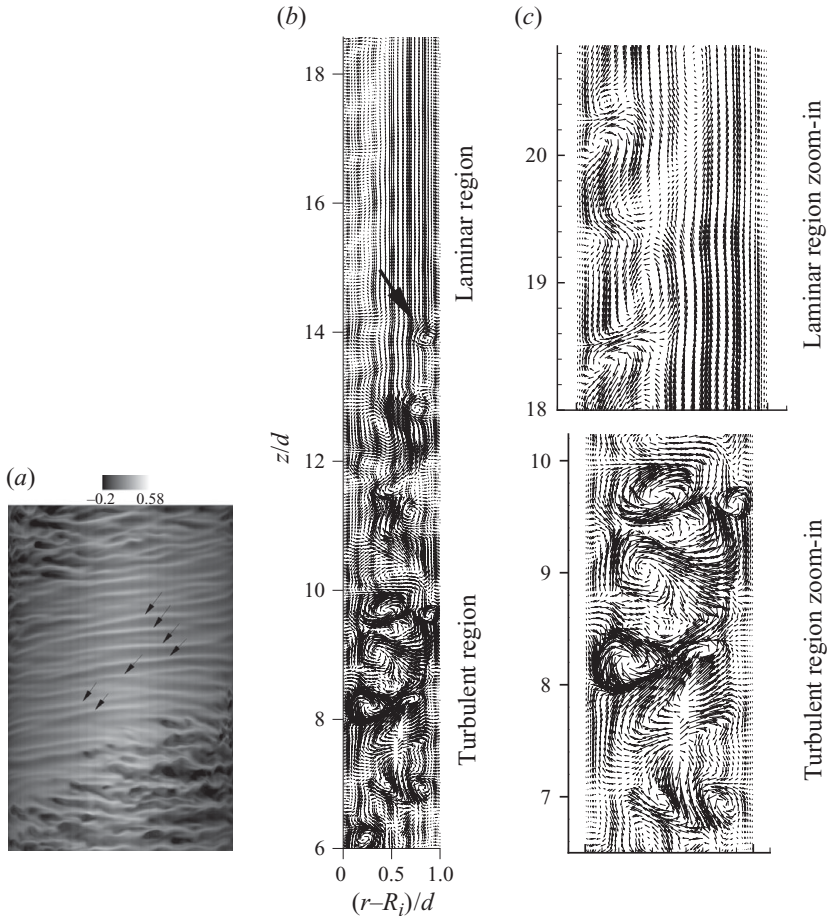


FIGURE 8. Flow patterns ($Re_i = 700$): (a) contours of azimuthal velocity in a grid surface near the inner wall; arrows in the plot indicate outflow boundaries of near-wall vortices in the laminar region. (b) Velocity field patterns in a radial-axial plane. (c) Enlargements of parts of (b).

edge is located near the outer cylinder, and the one at the trailing edge is near the inner cylinder. These features in conditionally averaged statistics result from the distribution of the instantaneous turbulent vortices.

From the velocity field in figure 8(b), one can observe pairs of counter-rotating vortices in the laminar spiral region near the inner cylinder. These laminar vortices are confined to the linearly unstable layer, and appear much weaker than the vortices in the turbulent region. The long streaks observed in the laminar spiral region in figure 8(a) correspond to the outflow boundaries of these counter-rotating vortex pairs.

We next employ the method of Jeong & Hussain (1995) to explore the vortex structures of spiral turbulence in the three-dimensional space. In figure 9, we visualize the vortices at $Re_i = 611$ with the iso-surface of λ_2 , which denotes the intermediate eigenvalue of the tensor $\mathbf{S} \cdot \mathbf{S} + \mathbf{\Omega} \cdot \mathbf{\Omega}$ (\mathbf{S} and $\mathbf{\Omega}$ are, respectively, the symmetric and antisymmetric parts of the velocity gradient). One can observe from the perspective view of figure 9(a) that the turbulent spiral is comprised of a large number of small-scale azimuthally elongated vortices. These vortices align themselves and collectively form a helical band.

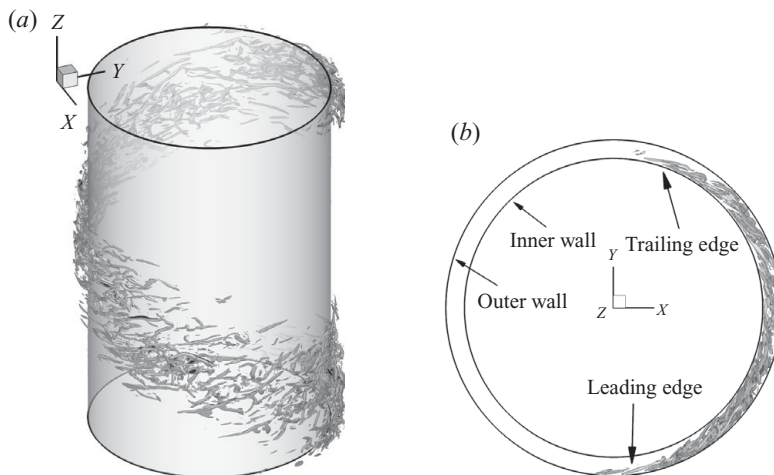


FIGURE 9. Vortices visualized by the iso-surface of the intermediate eigenvalue $\lambda_2 = -50.0$ ($Re_i = 611$, $Re_o = -1375$). (a) Perspective view, (b) top view. In (b), only vortices within the axial section $6.4 \leq z/d \leq 10.4$ have been shown.

Figure 9(b) is a top view (viewing towards the $-z$ direction) of the vortex structures. Here we have plotted only the vortex structures located in a short section of the domain in the axial direction, $6.4 \leq z/d \leq 10.4$, to demonstrate their azimuthal distribution. The shape of the region occupied by the vortices in the x - y plane remarkably resembles that of the mean turbulent-laminar interface geometry determined from the experiment by Van Atta (1966) and of the distribution of the conditional r.m.s. velocity magnitude from Dong (2009b). The region takes the shape of a ‘crescent moon’. At the trailing edge side, the vortices are confined to the inner portion of the gap and are inclined from the inner wall towards the bulk of flow, while at the leading edge they are confined to the outer portion of the cylinder gap. The characteristics of the vortex confinement, inclination and distribution and the examination of a time sequence of vortex visualizations suggest that these azimuthal vortices are originated from the inner cylinder wall. The vortices grow and detach from the inner cylinder to radially fill up the entire gap (figure 9b). Because the rotation velocity of the outer cylinder is considerably larger than that of the inner cylinder ($|U_o| \gtrsim 2|U_i|$), the vortices are subsequently convected along the azimuthal direction (clockwise) by the strong motion of the outer cylinder. This accounts for why the spiral pattern always rotates in the same direction as the outer cylinder.

It is suggested in Meseguer *et al.* (2009) that *axial* vortex filaments are generated near the inner cylinder based on the axial vorticity data in a horizontal plane. Our results and the vortex identification in the three-dimensional space indicate that the dominant vortices in spiral turbulence are the small-scale azimuthal vortices in the turbulent spiral region, and that no significant axial vortices seem evident. The axial vorticity filaments observed in Meseguer *et al.* (2009) are probably the footprints of the three-dimensional azimuthal vortices in the horizontal plane.

The small-scale vortices observed here in the turbulent spiral region are oriented predominantly along the azimuthal direction, which can be considered as the streamwise direction in the Taylor-Couette geometry. We note that the presence of streamwise vortices is a common phenomenon in turbulent spots and in fully developed turbulence. For example, in a flow visualization experiment on the turbulent

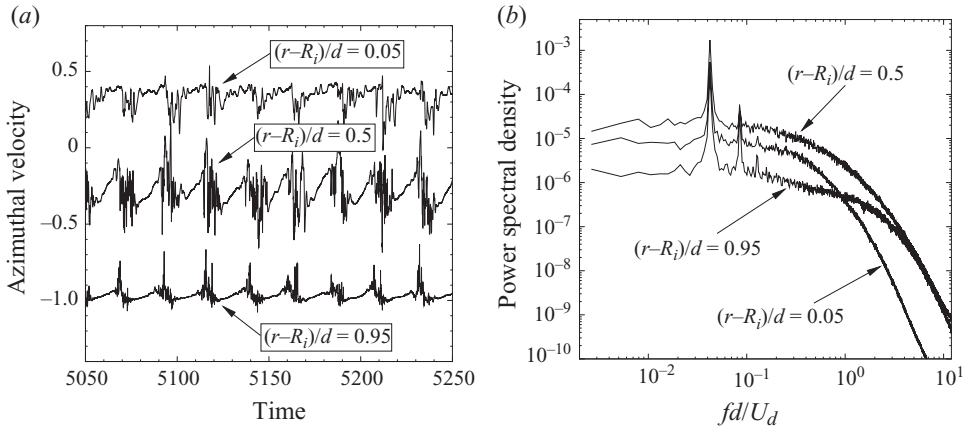


FIGURE 10. Time histories (a) and power spectrum (b) of the azimuthal velocity in the middle of the gap and at two points, respectively, near the inner and outer cylinders, at $Re_i = 611$.

spots in a plane Couette flow, Hegseth (1996) observes pervasive streamwise vortices; Dong (2007, 2008) shows in large-gap simulations (radius ratio 0.5) that the prevailing flow structures in fully developed Taylor–Couette turbulence are the small-scale azimuthal vortices.

We next examine the spectral characteristics of spiral turbulence. The bulk of the flow and the near-wall regions exhibit different characteristics and intensity in turbulent fluctuations. In figure 10(a), we show time histories of the azimuthal velocity at three fixed radial locations at $Re_i = 611$: a point in the middle of the cylinder gap and two points, respectively, near the inner and outer cylinder walls (at a distance $0.05d$ from the wall). From the velocity histories in the mid-gap and near the outer cylinder wall, one can clearly identify the turbulent and laminar phases. Near the inner cylinder wall, however, the differentiation of laminar and turbulent phases is less obvious. Small-amplitude fluctuations in the velocity signal can also be observed in the laminar phases near the inner cylinder, unlike in the mid-gap or near the outer cylinder. Such fluctuations are due to the laminar vortices on the inner cylinder surface (figure 8a) in the laminar spiral region.

Figure 10(b) compares the velocity power spectra at the three radial locations of figure 10(a). Note that the power spectral density has been averaged over the points along the axial direction with the same radial and azimuthal coordinates. The peaks in the power spectra correspond to the angular frequency, and its harmonics, of the spiral pattern revolving around the cylinder gap. One can observe the broadband feature in the spectral curves, characteristic of turbulent flows. The power spectral density in the mid-gap is notably higher than in the near-wall regions, suggesting that in spiral turbulence the strongest turbulent fluctuations are generally observed towards the core of the flow rather than in near-wall regions. The high-frequency component of the power spectrum near the outer cylinder essentially overlaps with that of the mid-gap, indicating that the high-frequency (small-scale) fluctuations, due to the sweep-through of the turbulent spiral, near the outer cylinder are as strong as in the mid-gap. The power spectral density near the inner cylinder, on the other hand, is notably lower than in the mid-gap at all frequencies. It is also lower than near the outer cylinder at high frequencies. But at low frequencies the spectral density is higher than near the outer cylinder, possibly owing to the fluctuations caused by the laminar vortices in the laminar spiral region on the inner wall. The low power spectral density

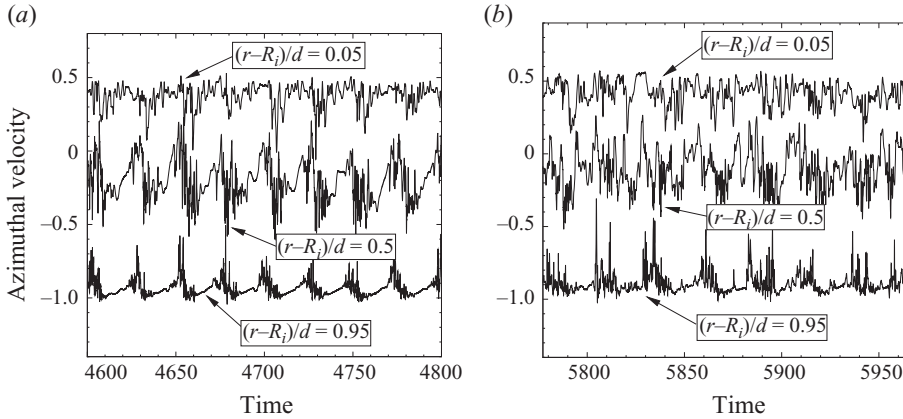


FIGURE 11. Transition from spiral turbulence to featureless turbulence: time histories of azimuthal velocity in the mid-gap and at two points near inner and outer cylinder walls at $Re_i = 700$ (a) and $Re_i = 800$ (b).

at high frequencies near the inner wall indicates that within the turbulent spiral region the turbulent fluctuation near the inner cylinder, i.e. generally towards the trailing edge (see figure 9b), is notably weaker than at the spiral core, and also weaker than near the outer cylinder, i.e. towards the leading edge.

As the inner-cylinder Reynolds number increases the spiral turbulence will transition to a turbulent state with no apparent large features (featureless turbulence). In different regions of the flow domain, our simulation shows, this transition to featureless turbulence does not take place simultaneously, but proceeds in succession from the inner cylinder to the outer cylinder with increasing Re_i . In figure 11, we plot time histories of the azimuthal velocity at three radial locations, the same as those in figure 10(a), at $Re_i = 700$ and 800. Comparison of the plots of figure 10(a) and figure 11 provides a sense of the sequence of transition at different radial locations in the domain. It suggests that as Re_i increases the transition to full turbulence progresses in succession from the inner wall towards the outer wall. In the region near the inner cylinder, as Re_i increases to 700 one can hardly distinguish the laminar and turbulent phases from the velocity history. The vicinity of the inner cylinder has virtually become turbulent at $Re_i = 700$. Towards the middle of the cylinder gap, on the other hand, the turbulent and laminar states obviously co-exist and alternate over time at $Re_i = 700$ (figures 11a and 5c). As Re_i is increased to 800, the mid-gap region has become turbulent with an apparent modulation in the turbulent intensity (figure 11b). For the region near the outer cylinder, on the other hand, at $Re_i = 800$ one can still distinguish the turbulent and ‘laminar’ phases from the velocity fluctuations (figure 11b). However, high-frequency fluctuations can also be observed during the ‘laminar’ phases at $Re_i = 800$, quite different from the situation at lower Reynolds numbers. These results clearly demonstrate a successive transition to full turbulence, from the inner cylinder to the outer cylinder, with the increase of Re_i . We note that the above-observed succession in transition to full turbulence is consistent with a comment in Van Atta (1966), which states that as Reynolds number increases the flow can be essentially fully turbulent near the inner cylinder and at mid-gap while near the outer cylinder it is still intermittent with turbulent and laminar fluid.

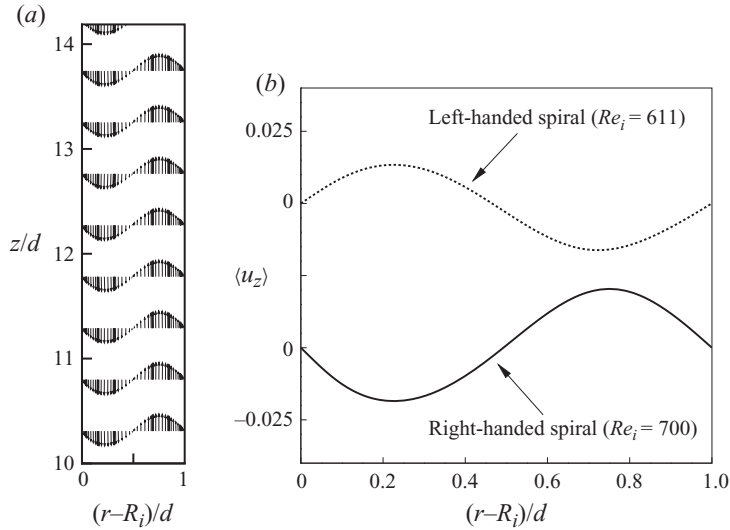


FIGURE 12. Mean flow. (a) Time-averaged mean velocity field in a radial-axial plane ($Re_i = 700$); for clarity velocity vectors are plotted only at several axial locations. (b) Profiles of mean axial velocity for left-handed ($Re_i = 611$) and right-handed ($Re_i = 700$) spirals.

4. Statistics of flow and turbulent spirals

We will next investigate the statistical features of spiral turbulence. The velocity field has been averaged over time, and for the profiles has also been averaged along the axial and azimuthal directions. We will refer to the flow statistics obtained with such a procedure as the *ordinarily averaged* statistics. Note that, because the turbulent spiral pattern revolves around the cylinder gap, direct averaging in time has smeared the contributions from the turbulent spirals in the ordinarily averaged flow statistics. Ordinarily averaged statistics, therefore, reflect the overall features of spiral turbulence over a long time. Note that this is very different from the *conditionally averaged* statistics explored in Dong (2009b). In Dong (2009b), the statistical features of the turbulent spiral have been extracted by employing conditional averaging techniques. The idea there is to follow the spiral pattern using a rotating reference frame, in which the pattern is essentially frozen in space so that its statistical features are exposed. We will compare features of the ordinarily averaged and the conditionally averaged flow statistics, and relate them to the instantaneous dynamical features observed in §3.

Let us first consider the mean flow characteristics. Figure 12(a) shows the ordinarily averaged mean velocity field in a radial-axial plane at $Re_i = 700$, which corresponds to a right-handed spiral (see figure 5c). For clarity only the velocity vectors at several discrete axial locations in a section of the cylinder height have been shown. The striking feature of the distribution is the predominant mean axial flow in the radial-axial plane and the opposing flow directions at different radial locations. For the right-handed spiral pattern at $Re_i = 700$, the mean velocity field is characterized by an axial flow in the positive z -direction in the outer portion of the cylinder gap, and an axial flow in the negative z -direction in the inner portion of the gap. This distribution character is reversed for a left-handed spiral pattern. Figure 12(b) compares profiles of the mean axial velocity, averaged in time and also along the axial and azimuthal directions, between a left-handed spiral pattern ($Re_i = 611$) and a right-handed spiral

pattern ($Re_i = 700$). For the left-handed spiral, in the radial–axial plane, the mean velocity is in the negative z -direction in the outer portion of the cylinder gap while in the inner portion it is in the positive z -direction.

The different distribution characteristics shown above for the ordinarily averaged mean axial velocity between a right-handed spiral and a left-handed spiral are related via a symmetry transform. Note that the incompressible Navier–Stokes equations, the continuity equation and the boundary conditions for the current problem are invariant under a reflection transform in z , that is

$$z \leftrightarrow -z, \quad u_z \leftrightarrow -u_z, \quad (4.1)$$

where u_z is the velocity component in the z -direction, while keeping the other coordinates and velocity components and the pressure unchanged. Under this transform, a solution with a left-handed spiral will be transformed to that with a right-handed spiral, and vice versa. Correspondingly, the distribution characteristics of the ordinarily averaged mean axial velocity of left- and right-handed spirals will be interchanged under this transform, as is evident from figure 12(b).

The layered distribution of the ordinarily averaged mean axial velocity shown in figure 12 is intimately related to the conditionally averaged statistical features of turbulent spirals. To understand this layered structure, let us take a close look at the conditionally averaged mean flow. In Dong (2009b), it is pointed out that the conditional mean flow axially always moves away from the core of a turbulent spiral and towards adjacent laminar spiral cores, and that this is a common feature of both left-handed and right-handed spirals. Our further observations indicate that the regions of positive and negative conditional mean axial flows have a skewed distribution towards either the outer or the inner cylinder walls, depending on the sense of handedness of the turbulent spiral.

To illustrate this point, in figure 13 we show the *conditional mean* axial velocity distribution at $Re_i = 700$, which corresponds to a right-handed spiral. Figure 13(a) plots the iso-surfaces at two levels, 0.02 and -0.02 , in three-dimensional space. Figures 13(b) and 13(c) plot contours of the conditional mean axial velocity in a radial–axial plane and in a horizontal x – y plane. Figure 13(b) is to be contrasted with a similar plot in the radial–axial plane in Dong (2009b) (figure 3a), but for a left-handed spiral. One can observe that the regions with positive and negative conditional mean axial velocities form two intertwined helical bands in three-dimensional space, the boundaries of which are located at the cores of the turbulent and laminar spirals. These two regions, when viewed in the radial–axial plane, are skewed towards either the inner or the outer wall (figure 13b). For a right-handed spiral, the region with the positive conditional mean axial velocity is skewed towards the outer wall (figure 13b) such that positive axial velocity tends to be observed at the outer cylinder in all axial locations except close to the turbulent spiral core. On the other hand, the region with negative conditional mean axial velocity is skewed towards the inner wall, and negative axial velocity tends to be observed there. The layered distribution of the conditional mean axial velocity in the cylinder gap is especially prominent in the laminar spiral core (figure 13c). For a left-handed spiral, this distribution characteristic is reversed; the region with positive conditional mean axial velocity is skewed towards the inner cylinder wall, while the region with negative velocity is skewed towards the outer wall; see figure 3(a) in Dong (2009b). We again note that these different distribution characteristics for left- and right-handed spirals are related with the reflection transform of (4.1).

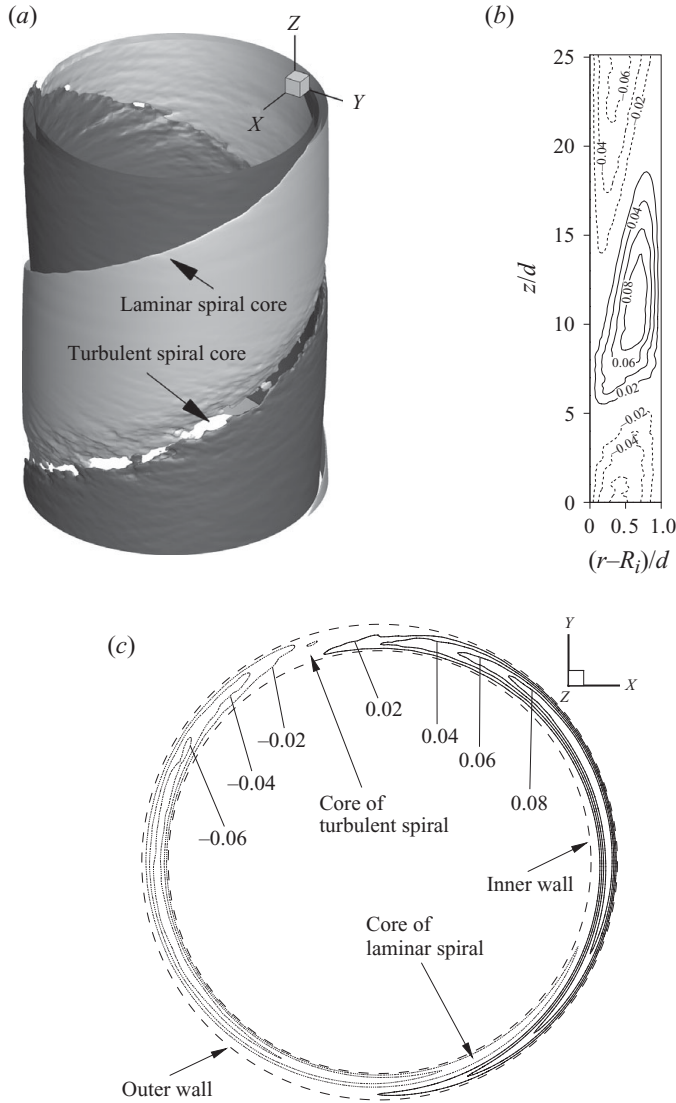


FIGURE 13. Conditional mean flow: iso-surfaces (a), and contours in a radial-axial plane (b) and in a horizontal plane (c), of the conditional mean axial velocity at $Re_i = 700$. In (a): light region, 0.02; dark region, -0.02 .

The skewed distribution of the conditional mean axial velocity indicates that, for a right-handed spiral, positive axial flows dominate the region near the outer wall while negative axial flows dominate the region near the inner wall. For a left-handed spiral, the reverse is true. As the spiral pattern propagates axially in the positive or negative directions, the long-term effect will be manifested as layered axial flows in positive or negative directions near the walls. This results in the layered distribution of the ordinarily averaged mean axial velocity as shown in figure 12.

It is interesting to note the differences in the time-averaged mean flow between the spiral turbulence regime and the fully developed Taylor-Couette turbulence at high Reynolds numbers. As discussed in Dong (2008), where a counter-rotating flow with a wide gap has been simulated with Reynolds numbers up to $Re_i = -Re_o = 4000$,

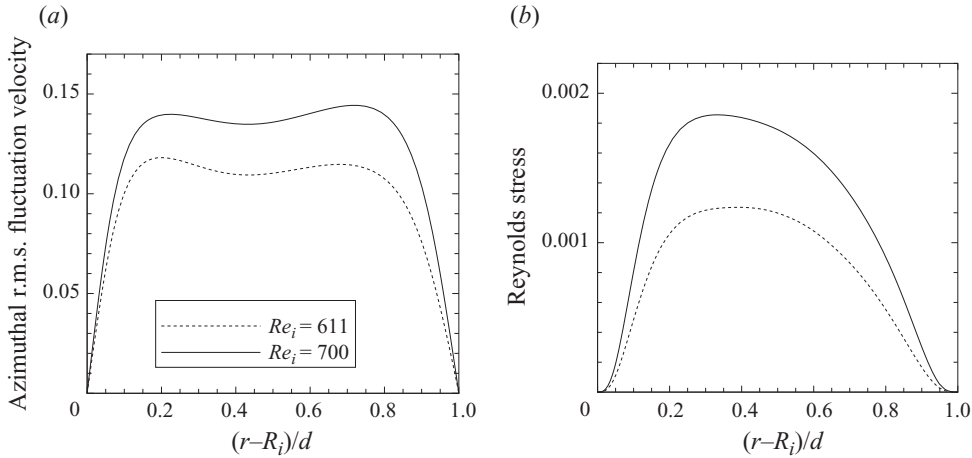


FIGURE 14. Comparison of profiles of r.m.s. azimuthal velocity u'_θ/U_d (a) and Reynolds stress $\langle u'_r u'_\theta \rangle / U_d^2$ (b) at different Reynolds numbers in the spiral turbulence regime.

the mean flow in fully developed turbulence exhibit regular pairs of large-scale Taylor vortices in the radial–axial plane, even though these vortices do not exist in the instantaneous sense. The mean axial velocity, when averaged along the axial direction, is therefore zero. In the spiral turbulence regime, on the other hand, the mean flow distribution in the radial–axial plane is very different, as shown in figure 12. The presence of regular spiral patterns and their propagation along the axial direction result in persistent axial flows of opposite directions in two separate regions of the cylinder gap.

In figure 14, we illustrate the characteristics of the fluctuation velocities in spiral turbulence obtained by ordinary time-averaging. Figure 14(a) compares profiles (across the cylinder gap) of the r.m.s. azimuthal velocity u'_θ between $Re_i = 611$ and 700. Increase in Re_i leads to increased r.m.s. fluctuation velocity in the entire cylinder gap, which is especially significant in the bulk of the flow. The r.m.s. azimuthal fluctuation velocity in the flow core ($0.2 \lesssim (r - R_i)/d \lesssim 0.8$) approximately has a constant value (with a slight dip near the mid-gap in the profile), which is much larger than in near-wall regions. This is consistent with the observed spectral characteristics in figure 10(b), where notably higher power spectral density has been found in the mid-gap compared to near-wall regions.

These features are related to the conditional velocity fluctuation characteristics investigated in Dong (2009b). Dong (2009b) has studied distributions of the conditionally averaged r.m.s. fluctuation velocity, and showed that the strongest turbulent intensity is associated with the core region of the turbulent spiral, with a slight bias towards its leading edge, and that there exists a notable asymmetry between the leading and trailing edges in terms of the turbulent intensity distribution. The fluctuation velocity distribution in figure 14(a) reflects the long-term effect of the turbulent spiral on the overall flow.

Figure 14(b) compares profiles of the ordinarily time-averaged Reynolds stress $\langle u'_r u'_\theta \rangle / U_d^2$, where u'_r is the radial fluctuation velocity, between $Re_i = 611$ and 700. One can observe positive Reynolds stress values across the cylinder gap, which in this sense is similar to the fully developed turbulence at higher Reynolds numbers; see Dong (2008). As explained in Dong (2008), the positivity is due to the fact

that small-scale azimuthal vortices tend to promote a positive correlation between the radial and azimuthal fluctuation velocities in the Taylor–Couette geometry. The peak Reynolds stress is located near the mid-gap but shifted towards the inner half, approximately at $0.25 \lesssim (r - R_i)/d \lesssim 0.5$. With increasing Re_i the peak location appears to shift further towards the inner portion of the cylinder gap. The peak location approximately coincides with the upper edge of the region near the inner wall, to which the laminar azimuthal vortices are confined in the laminar spiral (see figure 8). As shown in § 3, the small-scale vortices in the turbulent spiral region occupy the entire gap, thus promoting a positive Reynolds stress in the whole domain. On the other hand, the azimuthal vortices in the laminar spiral region are confined to the inner portion of the gap, enhancing the Reynolds stress in this region. The combined effect of the turbulent and laminar vortices contributes to a Reynolds stress distribution that peaks towards the inner portion of the cylinder gap.

5. Concluding remarks

In this paper, we have investigated several aspects of the dynamics and ordinarily time-averaged statistics of spiral turbulence employing three-dimensional direct numerical simulations. We have focused on two inner-cylinder Reynolds numbers, $Re_i = 611$ and 700 , with a fixed outer-cylinder Reynolds number $Re_o = -1375$, which in the current simulations correspond to left-handed or right-handed spirals.

The spiral turbulence phenomenon was first observed in the 1960s, and its barber-pole-like pattern was famously commented on by Feynman (Feynman 1964). A significant amount of knowledge about spiral turbulence has been gained since then. The phenomenon generally occurs in counter-rotating systems with a larger outer-cylinder Reynolds number, but has also been observed with a fixed inner cylinder or even co-rotating systems (Coles 1965). For a fixed outer-cylinder Reynolds number in a range of moderate values, as the inner-cylinder Reynolds number increases the flow will generally go through regimes of interpenetrating laminar spirals, turbulent bursts, spiral turbulence and featureless turbulence (Andereck *et al.* 1986). Spiral patterns may have a right or left helicity, with equal probability (Goharzadeh & Mutabazi 2001). Hysteresis has been noted with the phenomenon (Coles 1965; Andereck *et al.* 1986). The pitch angle of the spiral pattern may vary along the axial direction under different endwall conditions in experiments (Hegseth *et al.* 1989; Goharzadeh & Mutabazi 2008). The shape of the turbulent spiral in a horizontal plane resembles that of a crescent moon, with an asymmetry between the leading and trailing edges in terms of their shape, turbulent intensity distribution, and proximity to the walls (Van Atta 1966; Dong 2009*b*). A large-scale mean velocity gradient has been observed to persist along the azimuthal direction across both the turbulent and laminar spiral regions (Dong 2009*b*).

The present simulation has provided several additional findings about the spiral turbulence.

First, the turbulent spiral is comprised of numerous small-scale azimuthally elongated vortices. These vortices align into and collectively form a spiral in three-dimensional space. The azimuthal vortices originate from the inner cylinder wall around the trailing edge of the turbulent spiral. They spread into the entire gap while being convected along the azimuthal direction under the motion of the outer cylinder, and are distributed near the outer wall towards the leading edge of the turbulent spiral. The region occupied by these instantaneous vortices, in the horizontal plane (figure 9*b*), has the same shape (‘crescent moon’) and wall proximity as the

cross-section of the turbulent spiral determined by Van Atta (1966) from experiments and by Dong (2009*b*) from simulations.

The laminar spiral region is not void of vortices. Pairs of azimuthal vortices can be observed in the linearly unstable region near the inner cylinder surface. These laminar vortices contribute to the peak Reynolds stress observed towards the upper edge of this region.

Second, in spiral turbulence the turbulent fluctuations in the bulk of the flow are more energetic than in the near-wall regions at all frequencies. The high-frequency component of the velocity fluctuation near the outer cylinder has an intensity comparable to that in the mid-gap. The velocity fluctuation near the inner cylinder, on the other hand, generally lacks a significant high-frequency component when compared to that near the outer cylinder or in the mid-gap.

Third, the ordinarily time-averaged mean flow of spiral turbulence is characterized in the radial–axial plane by two layers of axial flows in opposite directions. The directions of the two axial-flow layers with a left-handed spiral are opposite to those with a right-handed spiral.

Lastly, as the inner-cylinder Reynolds number increases the transition from spiral turbulence to featureless turbulence does not take place simultaneously in the whole flow, but rather proceeds in succession from the inner cylinder to the mid-gap, and to the outer cylinder.

Finally, we would like to comment on the mean flow diagrams in Coles & Van Atta (1966) (figure 6) and in a recent study of the laminar–turbulent pattern in the plane-Couette flow by Barkley & Tuckerman (2007) (figure 8). The results in Coles & Van Atta (1966) suggest that the mean flow entering the turbulent region is almost normal to the turbulent–laminar interface, whereas the mean flow out of the turbulent region is in a direction nearly parallel to the turbulent–laminar interface. On the other hand, the results of Barkley & Tuckerman (2007) suggest a different relative orientation of the mean flow with respect to the turbulent–laminar interfaces, in which the mean flow appears to enter the turbulent region more gradually while leaving the region more abruptly. Our results with the conditionally averaged mean flow suggest a relative orientation of the mean flow with respect to the turbulent–laminar interface that is consistent with the result of Barkley & Tuckerman (2007). We note that Coles & Van Atta (1966) stated that in their experiment the measured axial velocity included a contribution from the azimuthal velocity gradient due to the particular configuration of the probe; see Coles & Van Atta (1966, footnote on p. 1970). It is not clear how and to what degree this factor may affect the observed relative orientation of the mean flow with respect to the interface. Future experiments on spiral turbulence can resolve this question concerning the relative relationship between the mean flow and the turbulent–laminar interfaces.

This work is partially supported by NSF. Computer time was provided by the TeraGrid through a TRAC grant.

REFERENCES

- ANDERECK, C. D., LIU, S. S. & SWINNEY, H. L. 1986 Flow regimes in a circular Couette system with independently rotating cylinders. *J. Fluid Mech.* **164**, 155–183.
- BARKLEY, D. & TUCKERMAN, L. S. 2005 Computational study of turbulent laminar patterns in Couette flow. *Phys. Rev. Lett.* **94**, 014502.

- BARKLEY, D. & TUCKERMAN, L. S. 2007 Mean flow of turbulent–laminar patterns in plane Couette flow. *J. Fluid Mech.* **576**, 109–137.
- BERGE, P., POMEAU, Y. & VIDAL, C. 1984 *Order Within Chaos*. Wiley.
- BOTTIN, S., DAVIAUD, F., MANNEVILLE, P. & DAUCHOT, O. 1998 Discontinuous transition to spatiotemporal intermittency in plane Couette flow. *Europhys. Lett.* **43**, 171–176.
- COLES, D. 1965 Transition in circular Couette flow. *J. Fluid Mech.* **21**, 385–425.
- COLES, D. & VAN ATTA, C. 1966 Progress report on a digital experiment in spiral turbulence. *AIAA J.* **4**, 1969–1971.
- COLES, D. & VAN ATTA, C. 1967 Digital experiment in spiral turbulence. *Phys. Fluids Suppl.* pp. S120–S121.
- COLOVAS, P. W. & ANDERECK, C. D. 1997 Turbulent bursting and spatiotemporal intermittency in the counter-rotating Taylor–Couette system. *Phys. Rev. E* **55**, 2736–2741.
- COUGHLIN, K. & MARCUS, P. S. 1996 Turbulent bursts in Couette–Taylor flow. *Phys. Rev. Lett.* **77**, 2214–2217.
- CROS, A. & GAL, P. LE 2002 Spatiotemporal intermittency in the torsional Couette flow between a rotating and a stationary disk. *Phys. Fluids* **14**, 3755–3765.
- CROSS, M. C. & HOHENBERG, P. C. 1993 Pattern formation outside of equilibrium. *Rev. Mod. Phys.* **65**, 851–1112.
- DONG, S. 2007 Direct numerical simulation of turbulent Taylor–Couette flow. *J. Fluid Mech.* **587**, 373–393.
- DONG, S. 2008 Turbulent flow between counter-rotating concentric cylinders: a direct numerical simulation study. *J. Fluid Mech.* **615**, 371–399.
- DONG, S. 2009a Direct numerical simulation of spiral turbulence. In *16th International Couette–Taylor Workshop*. Princeton, NJ.
- DONG, S. 2009b Evidence for internal structures of spiral turbulence. *Phys. Rev. E* **80**, 067301.
- DONG, S. & KARNIADAKIS, G. E. 2004 Dual-level parallelism for high-order CFD methods. *Parallel Comput.* **30**, 1–20.
- DONG, S. & KARNIADAKIS, G. E. 2005 DNS of flow past a stationary and oscillating cylinder at $Re = 10000$. *J. Fluid Struct.* **20**, 519–531.
- DONG, S., KARNIADAKIS, G. E., EKMEKCI, A. & ROCKWELL, D. 2006 A combined direct numerical simulation–particle image velocimetry study of the turbulent near wake. *J. Fluid Mech.* **569**, 185–207.
- DONG, S., KARNIADAKIS, G. E. & KARONIS, N. T. 2005 Cross-site computations on the TeraGrid. *Comput. Sci. Engng* **7**, 14–23.
- ECKHARDT, B., GROSSMANN, S. & LOHSE, D. 2007 Torque scaling in turbulent Taylor–Couette flow between independently rotating cylinders. *J. Fluid Mech.* **581**, 221–250.
- FEYNMAN, R. P. 1964 *Lectures in Physics*, vol. 2. Addison-Wesley.
- GOHARZADEH, A. & MUTABAZI, I. 2001 Experimental characterization of intermittency regimes in the Couette–Taylor system. *Eur. Phys. J. B* **19**, 157–162.
- GOHARZADEH, A. & MUTABAZI, I. 2008 The phase dynamics of spiral turbulence in the Couette–Taylor system. *Eur. Phys. J. B* **66**, 81–84.
- HEGSETH, J. J. 1996 Turbulent spots in plane Couette flow. *Phys. Rev. E* **54**, 4915–4923.
- HEGSETH, J. J., ANDERECK, C. D., HAYOT, F. & POMEAU, Y. 1989 Spiral turbulence and phase dynamics. *Phys. Rev. Lett.* **62**, 257–260.
- JEONG, J. & HUSSAIN, F. 1995 On the identification of a vortex. *J. Fluid Mech.* **285**, 69–94.
- KARNIADAKIS, G. E., ISRAELI, M. & ORSZAG, S. A. 1991 High-order splitting methods for the incompressible Navier–Stokes equations. *J. Comput. Phys.* **97**, 414–443.
- LEPILLER, V., PRIGENT, A., DUMOUCHEL, F. & MUTABAZI, I. 2007 Transition to turbulence in a tall annulus submitted to a radial temperature gradient. *Phys. Fluids* **19**, 054101.
- LITSCHKE, H. & ROESNER, K. G. 1998 New experimental methods for turbulent spots and turbulent spirals in the Taylor–Couette flow. *Exp. Fluids* **24**, 201–209.
- MARQUES, F., MESEGUER, A., MELLIBOVSKY, F. & AVILA, M. 2009 Spiral turbulence in counter-rotating Taylor–Couette flow. In *16th International Couette–Taylor Workshop*. Princeton, NJ.

- MESEGUER, A., MELLIBOVSKY, F., AVILA, M. & MARQUES, F. 2009 Instability mechanisms and transition scenarios of spiral turbulence in Taylor–Couette flow. *Phys. Rev. E* **80**, 046315.
- PRIGENT, A., GREGOIRE, G., CHATE, H., DAUCHOR, O. & VAN SAARLOOS, W. 2002 Large-scale finite-wavelength modulation with turbulent shear flows. *Phys. Rev. Lett.* **89**, 014501.
- PRIGENT, A., GREGOIRE, G., CHATE, H. & DAUCHOT, O. 2003 Long-wavelength modulation of turbulent shear flows. *Physica D* **174**, 100–113.
- VAN ATTA, C. 1966 Exploratory measurements in spiral turbulence. *J. Fluid Mech.* **25**, 495–512.